Ultrasound-Assisted Synthesis of Mesoporous Zirconia-Hydroxyapatite Nanocomposites and Their Dual Surface Affinity for Cr 3+ /Cr 2 O 7 2– Ions

Karima Achelhi, Sylvie Masse, Guillaume Laurent, Cécile Roux, Abdelaziz Laghzizil, Ahmed Saoiabi, Thibaud Coradin

Ultrasound-assisted synthesis of mesoporous zirconia-hydroxyapatite nanocomposites and their dual surface affinity for $Cr^{3+}/Cr_2O_7^{2-}$ ions

Karima Achelhi,[¥,‡] Sylvie Masse,[¥] Guillaume Laurent,[¥] Cécile Roux,[¥] Abdelaziz Laghzizil,[‡] Ahmed Saoiabi,[‡] and Thibaud Coradin[¥,]*

[¥]UPMC-P6 ; CNRS, Chimie de la Matière Condensée de Paris, Collège de France, 75005 Paris, France, and [‡]Laboratoire de Chimie Physique Générale, Faculté des Sciences-Université Mohamed V-Agdal, BP.1014 Rabat, Morocco.

thibaud.coradin@upmc.fr

RECEIVED DATE (to be automatically inserted after your manuscript is accepted if required according to the journal that you are submitting your paper to)

* Thibaud Coradin, a-mail: thibaud.coradin@upmc.fr; tel: + 33-144271527; fax; +33-1-44271443.

ABSTRACT: Zirconia-hydroxyapatite nanocomposites were prepared by sol-gel deposition of zirconium oxide from a zirconium alkoxide in the presence of apatite colloidal suspension under ultrasonication. The material porosity evolves from mainly microporous zirconia to mesoporous hydroxyapatite, with decreasing surface area and increasing pore volume. XRD studies indicate that the apatite phase is well-preserved within the composite materials. The homogeneous dispersion of apatite colloids within the zirconia network was supported by TEM observations and nitrogen sorption

measurements. ^{31}P solid-state NMR studies suggest that partial dissolution of apatite may have occured during the preparation, leading to the adsorption of phosphate species on zirconia particles. This is confirmed by XRD studies of nanocomposites after thermal treatment that demonstrate the preferred formation of tetragonal over monoclinic ZrO_2 in the presence of hydroxyapatite. In order to investigate the surface properties of these novel materials, the adsorption of Pb^{2+}, Cr^{3+} and $Cr_2O_7^{2-}$ was evaluated. Metal cations were preferentially adsorbed on apatite-rich composites whereas $Cr_2O_7^{2-}$ shows a good affinity for the zirconia-rich phases. Zirconia-apatite materials showed the most promising performance in terms of recyclability. These nanocomposites that combine microporosity, mesoporosity and dual sorption properties for these species appear as interesting materials for metal ion remediation and may also find applications as biomaterials.

1. INTRODUCTION

Hydroxyapatite $Ca_{10}(PO_4)_6(OH)_2$ is a mineral, mainly of biogenic origin, with a complex bulk and surface reactivity, including cation-exchange, phosphate and hydroxyl substitution, Lewis and Bronsted acid/base reactivity.[1-4] Moreover, at the nanoscale, hydroxyapatite exhibits an hydrated amorphous calcium phosphate (ACP) layer,[5-10] with high dissolution/exchange capacity.[11-13] Such a strong reactivity has a major impact in vivo as it may be involved in the fixation of metal ions in bone with severe pathological implications.[14-16] In parallel, it is possible to take benefits of metal-apatite affinity in the field of environmental remediation.[17,18]

The association of hydroxyapatite with metal oxides for biomedical purposes has already been widely described in the literature.[19] In particular, silica-,[20-22] alumina-,[23-25] titania-[26-28] and zirconia-based[29-31] composites have been studied for the design of bioceramics mainly due to their enhanced chemical and mechanical stability compared to the pure apatite phase. In contrast, very few studies considered the application of such materials as sorbents.[32-34] Such apatite-based composites are easily accessible in a dense form starting from mixture of metal oxide and apatite micrometric or nanometric powders via high pressure/temperature treatments[35,36] or spark plasma sintering.[37,38] However, the access to porous materials is of primary importance for the design of biomedical scaffold or for remediation purpose. In

this situation, soft chemistry routes may be preferred but they face a real challenge due to various conditions of formation and stability of the apatite and metal oxide phases. For instance, calcium ions easily form stable phases with metal oxides, such as $CaSiO_4$,[39] $CaTiO_3$,[40] or $CaZrO_3$[41] whereas phosphate ions have also a strong affinity for transition metal cations. Therefore several byproducts may be formed when preparation is performed from ionic precursors. Another key parameter is related to the different pH ranges of formation or stability. In particular, hydroxyapatite is easily converted into β-tricalcium phosphate phase if pH conditions are too acidic.[1,2] Finally, colloidal approaches are limited by the poor dispersion of apatite nanoparticles in solution that require surface modification to achieve suitable stability.[42-45]

In this work, we describe a novel alternative sol-gel-based approach relying on the *in situ* formation of a metal oxide gel from a metal alkoxide, in the presence of pre-formed apatite nanoparticles. We selected zirconia due to its high chemical and mechanical stability and wide applications in the field of biomaterials.[46] Alternative soft chemistry route were proposed either based on the precipitation of apatite in the presence of pre-formed ZrO_2 colloids or on apatite-zirconia co-precipitation, but these approaches were limited to low zirconia content.[47,48] The reaction was performed under sonication to insure a good dispersity of the apatite colloids prior gelation. These materials are micro- and mesoporous over a wide range of composition, which make them promising materials for biomedical applications.[19] In terms of surface properties, they very interestingly combine the affinity of apatite for cationic species and that of ZrO_2 for polyanions, making them the first materials to date with good binding properties for both Cr^{3+} and $Cr_2O_7^{2-}$ ions, a promising property for future developments in metal remediation processes.[49]

2. EXPERIMENTAL SECTION

2.1. Nanocomposite synthesis. The apatite powder (HAp) was prepared by neutralization of $Ca(OH)_2$ with $NH_4H_2PO_4$ in water following a previously-described procedure.[50] Addition of 0 to 3.268 g of the apatite powder to 12 mL of a 20 wt% $Zr(OCH(CH_3)_2)_4$ solution in 1-propanol[51] was performed under sonication in a X-tra 35 kHz thermostated ultrasound bath (from Fisher Bioblock) at a working

power of 160 W for 30 minutes. Then, ammonium hydroxide (30 wt% in water) was added dropwise until pH 10.5 and sonication was left to proceed over 90 minutes. The resulting precipitates were recovered by centrifugation, thoroughly washed with deionized water and dried overnight in an oven operating at 120°C. Samples were named after the ZrO_2:HAp weight ratio *ZH* (see Table 1). Further thermal treatments were performed at 900°C.

Table 1. Apatite content (HAp), specific surface area (S_{BET}), porous volume (V_p) and average pore size (D_p) from BJH model and average micropore size (D_m) from HK model of pure phases (ZrO_2, HAp) and nanocomposites

Sample	HAp (g)	S_{BET} ($m^2.g^{-1}$)	V_p ($cm^3.g^{-1}$)	D_p (nm)	D_m (nm)
ZrO_2	0	293	0.19	1.2	0.84
ZH4	0.204	293	0.26	1.2	0.66
ZH2	0.408	296	0.30	1.2	0.56
ZH1	0.817	267	0.32	1.8	0.54
ZH0.5	1.634	235	0.38	1.8	0.56
ZH0.25	3.268	218	0.39	1.8	0.46
HAp	-	102	0.54	6.9	0.46

2.2. Characterizations. The behaviour of apatite colloids in solution was studied by Dynamic Light Scattering (DLS) performed on a ZetaPlus equipment (Brookhaven Instruments Inc.)**.** The crystalline phases were identified using a powder X-ray diffractometer (XRD) (Philips PW131 diffractometer). The N_2 adsorption-desorption isotherms for dried powders were obtained by multi-point N_2 gas sorption experiments at 77 K using a Belsorb instrument. The specific surface areas were calculated according to the Brunauer–Emmett–Teller (BET) method using adsorption data in the relative pressure range from 0.05 to 0.25. The average pore size was estimated using the Horvath-Kawazoe (HK) model in the

microporous range while pore volume and pore size distribution were determined using the Barret–Joyner–Halenda (BJH) approximation in the mesoporous range. Scanning electron microscopy (SEM) was performed on gold-coated powders on a JEOL JSM-5510LV operating at 20 kV. Transmission electron microscopy (TEM) was performed on a Tecnai Spirit G2 operating at 100 kV.

Solid-state MAS NMR studies were performed on an Avance III 700 Bruker spectrometer at a frequency of 283.42 MHz for ^{31}P nucleus. Spectra were recorded using a 3.2 mm trigamma Bruker probe (MAS frequency, 14 kHz). In the case of Cross-Polarization (CP MAS) and HPDec MAS experiments, High Power Decoupling was applied during acquisition (spinal 64, ν_{1H}=50 kHz). $\{^1H\}$-^{31}P HPDec MAS NMR spectra were recorded using 30° pulse, recycle delay of 10 s and NS, 128. $\{^1H\}$-^{31}P CP-MAS NMR experiments were carried out using 90° pulse, recycle delay of 3 s, a contact time t_{CP} of 2 ms and NS, 280, except for time variation experiments where t_{CP} varies from 0.1 ms to 10 ms and NS, 560. A line broadening (LB) of 10 Hz was applied for both $\{^1H\}$-^{31}P HPDec MAS and CP MAS spectra processing.

2.3. Metal-binding experiments. Metal ion solutions with concentrations ranging from 0 to 1000 $mg.L^{-1}$ were prepared from $Pb(II)NO_3$, $Cr(NO_3)_3.9H_2O$ and $K_2Cr_2O_7$ salts dissolved in distilled water at pH 5, pH 4 and pH 3 (adjusted with HNO_3), respectively, to assure full dissolution. This range of concentration was selected to include commercial wastewaters content (10-20 $mg.L^{-1}$)[52] and was extended to higher concentrations to determine full sorption isotherms. 0.2 g of the different materials were added to 100 mL of these solutions and stirred at 25°C over 3 h (lead) or 6 h (chromium) to reach sorption equilibrium. After centrifugation, the metal content of the supernatant was determined by ICP.

Isotherms were analyzed using the non-linear fitting of experimental points with the Langmuir equation (eq. 1):

$$q_e = \frac{q_{e,max} K C_e}{1 + K C_e} \quad (1)$$

where q_e is the amount of sorbed metal at equilibrium ($mg.g^{-1}$), $q_{e,max}$ is the maximum sorption capacity ($mg.g^{-1}$), K is the equilibrium constant of the adsorption reaction and C_e is the equilibrium concentration of metals remaining in solution ($mg.L^{-1}$)

Recycling experiments were performed from materials previously put in contact with 25 $mg.L^{-1}$ solutions of $Cr(NO_3)_3.9H_2O$ and $K_2Cr_2O_7$ in acidic conditions, as decribed above (first adsorption step). The resulting wet powders were placed in 100 mL of deionized water with pH adjusted to 9 and 11 (with NaOH) overnight. After centrifugation, the supernatant was analyzed by ICP (first desorption step). The recovered powders were dried overnight at 100°C and used for a second round of adsorption/desorption steps. The desorption rate was calculated as the ratio of metal in the supernatant over the metal content of the sorbent after adsorption. The second adorption rate was calculated as the ratio of metal on the sorbent after the second adsorption experiment over the metal content of the sorbent after desorption.

3. RESULTS AND DISCUSSION

3.1. Preparation of the nanocomposites. In order to set up the synthesis protocol for ZrO_2-HAp nanocomposites, we first hypothesized that a co-precipitation of ZrO_2 and HAp from ionic and molecular precursors would lead to the formation of zirconium phosphate or calcium zirconate as byproducts. For this reason, we decided to start from HAp nanopowder dispersion and induce ZrO_2 formation through a sol-gel process. However, bare HAp sols are prone to fast precipitation so we tried to perform the zirconia gel formation under sonication.

In a first step, the dispersion and stability of apatite particles in the solvent of the zirconium alkoxide precursor, i.e. 1-propanol, was studied by DLS. Solutions of apatite content varying from 0.1 $mg.mL^{-1}$ to 1 $mg.mL^{-1}$ were prepared and sonicated during 5 to 30 min. As shown in SI-1, large particle aggregates were evidence for concentrations above 0.5 $mg.mL^{-1}$ after 30 min and the settling time, as indicated by the decay of the diffusion signal intensity, occurred within 5 minutes post-sonication. In contrast, for a 0.25 $mg.mL^{-1}$ after 30 min, the main population consisted of colloids *ca*. 100 nm in size and was stable over 15 min.

The following issue of this process was to reach final HAp:ZrO_2 ratios in the 10-90 % range. A first series of attempts were made by keeping a fixed HAp content and varying the zirconium alkoxide concentration. However, it was observed that the presence of apatite colloids had a strong impact on the formation of the zirconia network, slowing down the kinetics of gel formation from a few minutes to several hours for the lowest zirconium alkoxide concentration. On this basis, the alkoxide concentration was fixed, variable amounts of apatite powders were added and their dispersion/stability was studied after 30 min of sonication. DLS analyses indicated that the presence of the zirconium alkoxide has a significant impact on the apatite dispersion after sonication although moderately impacting its stability (SI-1). For this reason sonication was maintained during the addition of the ammonium hydroxide solution. It is worth noting that similar sonication conditions have been previously reported for the preparation of yttrium-stabilized zirconia particles in ethanol.[53]

Under these conditions, zirconia gel formation occurred instantly, suggesting that the apatite particles are trapped within the ZrO_2 network. However, this gel was rapidly converted into a precipitate that settled if sonication was interrupted at this stage. Taking into account that the sol-gel reactions involve complex dissolution/reprecipitation, ripening and structural reorganization steps upon ageing, it was found more appropriate to maintain sonication over a longer time period (*i.e.* 90 min).

Taking all these parameters into account, the reaction was performed as summarized in Scheme 1. The apatite powder was added to the $Zr(OCH(CH_3)_2)_4$ in 1-propanol solution under sonication for 30 min to ensure the suitable dispersion of the particles. The mixture pH was then raised to pH 10.5 and sonication was continued. A gel was formed within the first minutes after ammonia addition that was converted into a particulate suspension. After 90 min sonication, a homogenous precipitate was recovered and dried at 120°C.

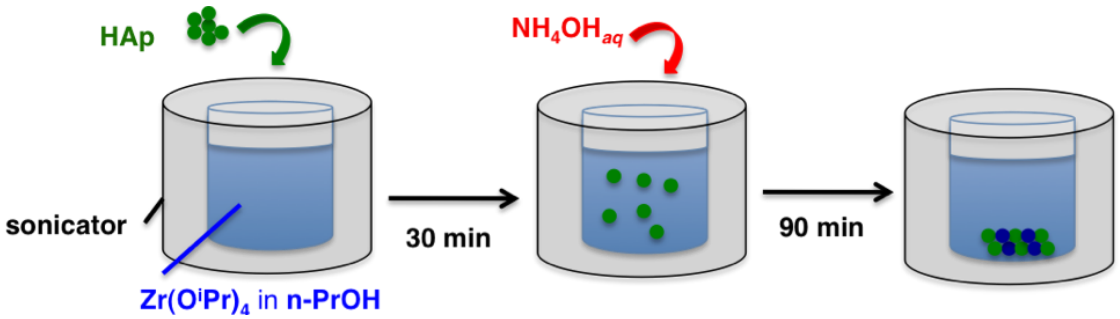

Scheme 1. Overview of the synthetic route to zirconia-hydroxyapatite (HAp) nanocomposites

3.2. Nanocomposite characterization. In a first step, the resulting powders were analyzed by XRD to check the influence of the synthetic procedure on the apatite structure and to identify the zirconium phase. As shown in Figure 1, the apatite-free powder exhibits a broad diffraction peak centered at 2θ = 31.5 ° together with two overlapping large signals at *ca*. 50° and 60°. It can be suggested that this corresponds to an amorphous precursor zirconium oxyhydroxide phase[54] or to ZrO_2 nanoparticles with very small coherence domains. As far as the initial HAp powder is concerned, its XRD diffractogram corresponds well with the expected features of the hydroxyapatite structure from the JCPDS file (09-0432). As the ZrO_2:HAp ratio increases, the diffraction peaks corresponding to the HAp structure become merged into the broad peaks of the zirconium phase. However, the most intense HAp peaks are still visible for the *ZH4* sample while no additional diffraction peaks appears, suggesting the preservation of the apatite structure in all conditions.

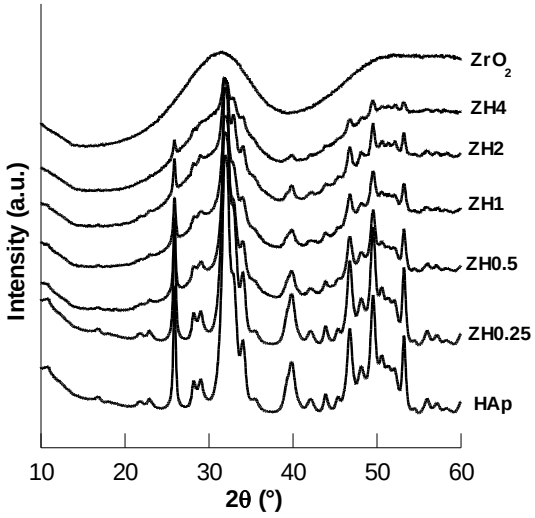

Figure 1. XRD diffractograms of ZrO_2, HAp and nanocomposites after overnight drying at 120°C

The nanocomposites were then investigated by electron microscopy to check the homogeneity of the samples and, more particularly, to study the dispersion of apatite colloids within the zirconia network. On the basis of SEM, the powders of apatite-free Zr phase and initial apatite were almost indiscernible, consisting of particle aggregates ranging from 100 nm to several microns (SI-2). As a result, SEM images of nanocomposite powders did not bring clear information about the material structure. In contrast, TEM images of pure phases were clearly distinct, as the ZrO_2 phase consists of large aggregates of amorphous particles *ca*. 10 nm in size whereas the apatite phase is composed of rod-like particles *ca*. 50 nm in length (Figure 2). The two morphologies are seen to co-exist in nanocomposite structure and, at higher magnification, it is possible to visualize apatite rods buried within the zirconia matrix (Fig. 2 and Fig. SI-3)

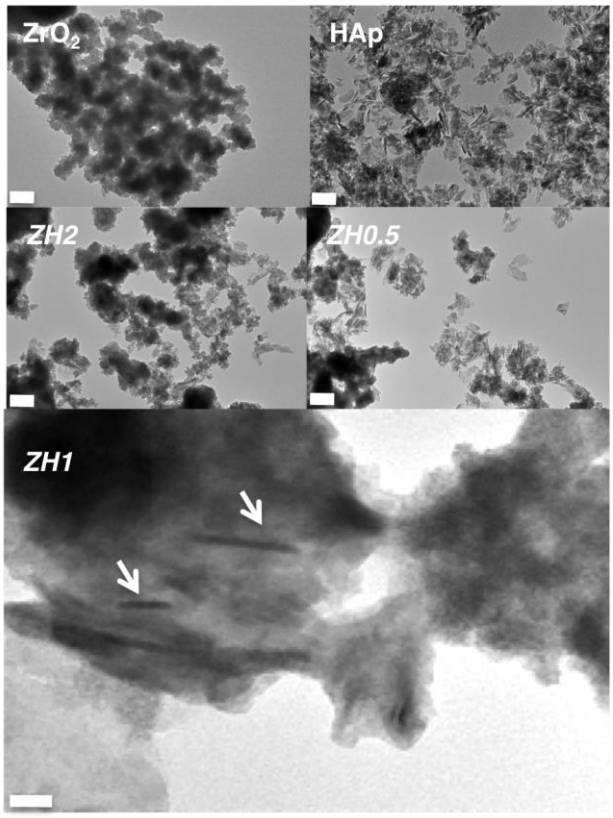

Figure 2. Selected TEM images of ZrO_2, HAp and nanocomposites (scale bar = 100 nm, except for *ZH1* where scale bar = 20 nm and arrows indicate apatite nanorods buried in the zirconia matrix)

In a step forward, the porous features of the nanocomposites were investigated (Figure 3). ZrO_2 and all composite materials exhibit a type IV hysteresis indicating that the nanocomposites exhibit mesoporosity.[55] (Fig. 3a and Fig. SI-4). The ZrO_2 phase shows a significant microporosity and narrow hysteresis. Low apatite content preserves the microporosity but some mesoporosity becomes more evident, as indicated by the widening of the hysteresis. With higher apatite content, the microporosity decreases and the mesoporosity increases. The isotherm of pure HAp appears as a limit case between type IV and type V isotherms, suggesting a weak interaction between nitrogen gas and the apatite surface.[55] Application of the BET and BJH models indicates that the ZrO_2 phase exhibits a large specific surface area (*ca*. 300 $m^2.g^{-1}$) and low porous volume (*ca*. 0.2 $cm^3.g^{-1}$) whereas HAp has a lower specific area (*ca*. 100 $m^2.g^{-1}$) but higher porous volume (*ca*. 0.55 $cm^3.g^{-1}$) (Table 1). Introduction of small apatite content within the Zr-phase does not modify the specific surface area but increases the porous volume. For *ZH1,* the specific surface area decreases whereas the porous volume reaches a plateau for *ZH2*. The composite obtained with the highest apatite content (80 w%) exhibit higher S_{BET} and lower V_p than the pure apatite. BJH distribution indicates that ZrO_2 structure has a pore size range below 2 nm whereas apatite introduction leads to the presence of a novel pore population centered at *ca*. 5 nm whose relative contribution to the total porous volume increases with apatite content (Fig 3b). As a comparison, the initial HAp powder exhibits a broad pore distribution centered at 9-10 nm. Indeed application of the BJH model to these systems suffers from two limitations. First, it is not fully adapted when microporosity is present. To overcome this problem, the sorption isotherms were also analyzed using the HK model. This method gives access to the average pore size distributions in the microporous range D_m that are reported in Table 1. These data clearly indicate that micropores are present in the materials, with size decreasing from *ca*. 0.85 nm to *ca*. 0.45 nm with increasing apatite content. Such a D_m value of *ca*. 0.45 nm is also found for pure HAp, suggesting that the apatite phase also exhibits some microporosity. Another limitation of the BJH model is that it considers a network of cylindrical pores that may not correspond to the structural complexity of the here-studied systems. To check this, we have used the model developed by Innes that can be applied to a parallel plate morphology.[56] As indicated in Table SI-

5, the results are very similar to those obtained through the BJH model, therefore validating our analyses of the materials in the mesoporous range. Overall, the incorporation of apatite particles introduce mesopores within the mainly microporous network of the zirconium phase. Noticeably, the narrow pore size distribution resulting from apatite particles suggest that they are homogeneously dispersed in the ZrO_2 matrix, in agreement with TEM data.

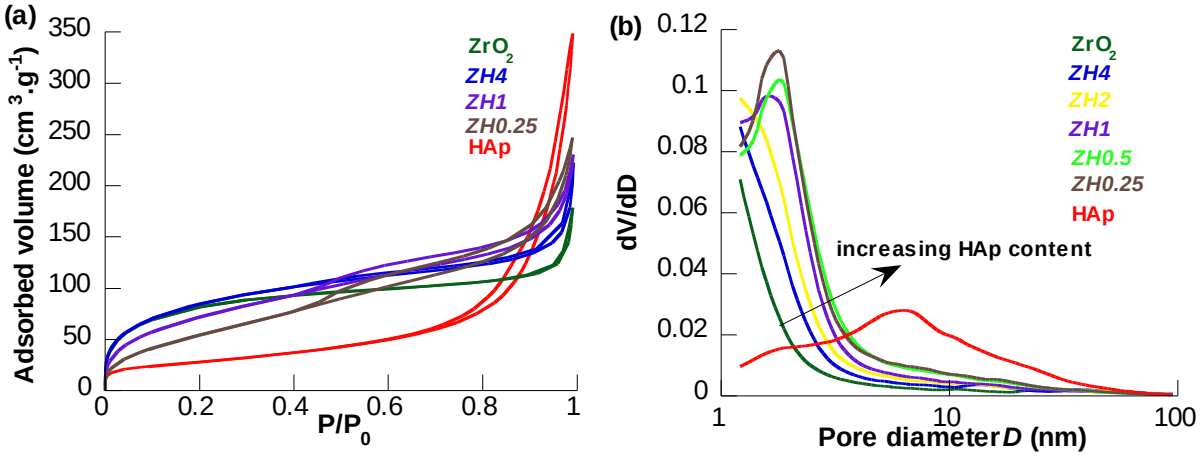

Figure 3. (a) N_2-sorption isotherms and (b) pore size distribution from BJH calculation for ZrO_2, HAp and selected nanocomposites

In a step further, it was important to investigate in more details the nature of the interface between ZrO_2 and apatite crystals using ^{31}P MAS NMR techniques (Figure 4). The $\{^1H\}$-^{31}P HPDec MAS spectra of the pure apatite shows a main peak at 2.7 ppm, characteristic of the phosphorus atom of phosphate groups in the apatite structure (Fig 4a).[5-10] A similar signal was obtained for all samples but its intensity decreases with decreasing apatite content (i.e. increasing *ZH*). In addition, a broad signal of low intensity was present in the 0-5 ppm region, in agreement with previous reports on phosphate groups located in the amorphous calcium phosphate layer (ACP) associated with nanocrystalline apatites.[5-10] Finally, for *ZH4*, additional signals were found in the (-20)-(-25) ppm region. Further analysis of this *ZH4* sample was performed by $\{^1H\}$-^{31}P CP MAS experiments at increasing contact time (Fig. 4b and SI-6). These experiments allow a better identification of the signals at -19.5 ppm, -20.5 ppm, -22.3 ppm and -24.7 ppm that have been reported to correspond to $H_2PO_4^-$ and/or HPO_4^{2-} adsorbed

on zirconia surfaces or forming $Zr(HPO_4).xH_2O$ phases.[57-59] The 0-5 ppm broad region was more clearly resolved with at least two peaks at *ca*. 0 and 3.5 ppm and an additional signal at – 4.2 ppm. Because these signals were not clearly evidenced in the $\{^1H\}$-^{31}P HPDec MAS spectra, they should correspond to protonated phosphate species, in particular HPO_4^{2-}, that have also been identified in the ACP layer.[5-10] This attribution could be supported by studying the variations of the intensity of the different signals as a function of contact time t_{CP} (Fig. 4c and Fig. SI-7).[6] All signals except the 2.7 ppm one exhibit a fast rise, indicating short P…H distances, as expected for $H_2PO_4^-$ and/or HPO_4^{2-} species, followed by a $T_{1\rho}$ relaxation-induced decay. In contrast, the 2.7 ppm signal of bulk apatite PO_4^{3-} groups shows continuous increase with t_{CP}, as expected for large P…H distances (*i.e.* interaction with the hydroxyl group of the HAp structure). Taken together, these data indicate that the *ZH4* sample contains phosphate groups belonging to the crystalline core and amorphous hydrated layer of HAp nanoparticles together with $H_2PO_4^-$ and/or HPO_4^{2-} groups interacting with Zr(IV) species. As no free phosphate group is present in the initial apatite suspension, they should originate from the dissolution of the apatite colloids during the material preparation process and become incorporated within, or are adsorbed on, the growing ZrO_2 colloids. Note that the precipitation of a zirconium phosphate phase cannot be put aside on the sole basis of the NMR data. One intriguing observation is that this phenomenon is only apparent for *ZH4*, *i.e.* for the highest zirconium:apatite ratio. Although this observation is difficult to explain at this time, it can be suggested that the zirconium species play an active role in the apatite dissolution process due to their high affinity for phosphate species.

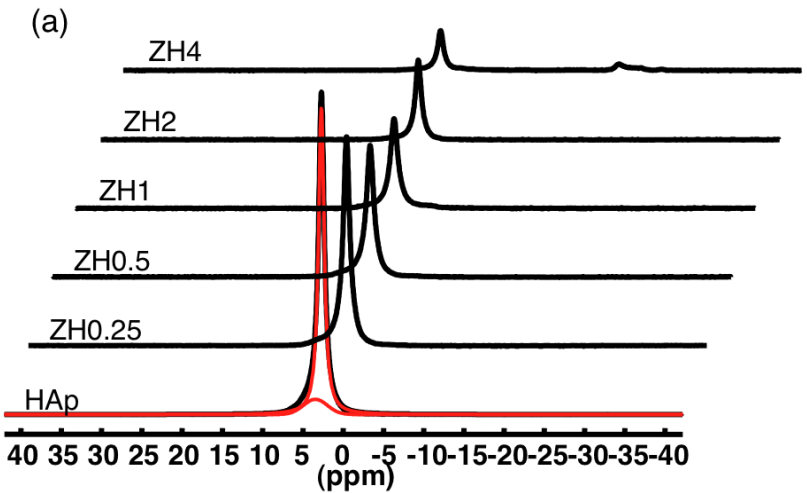

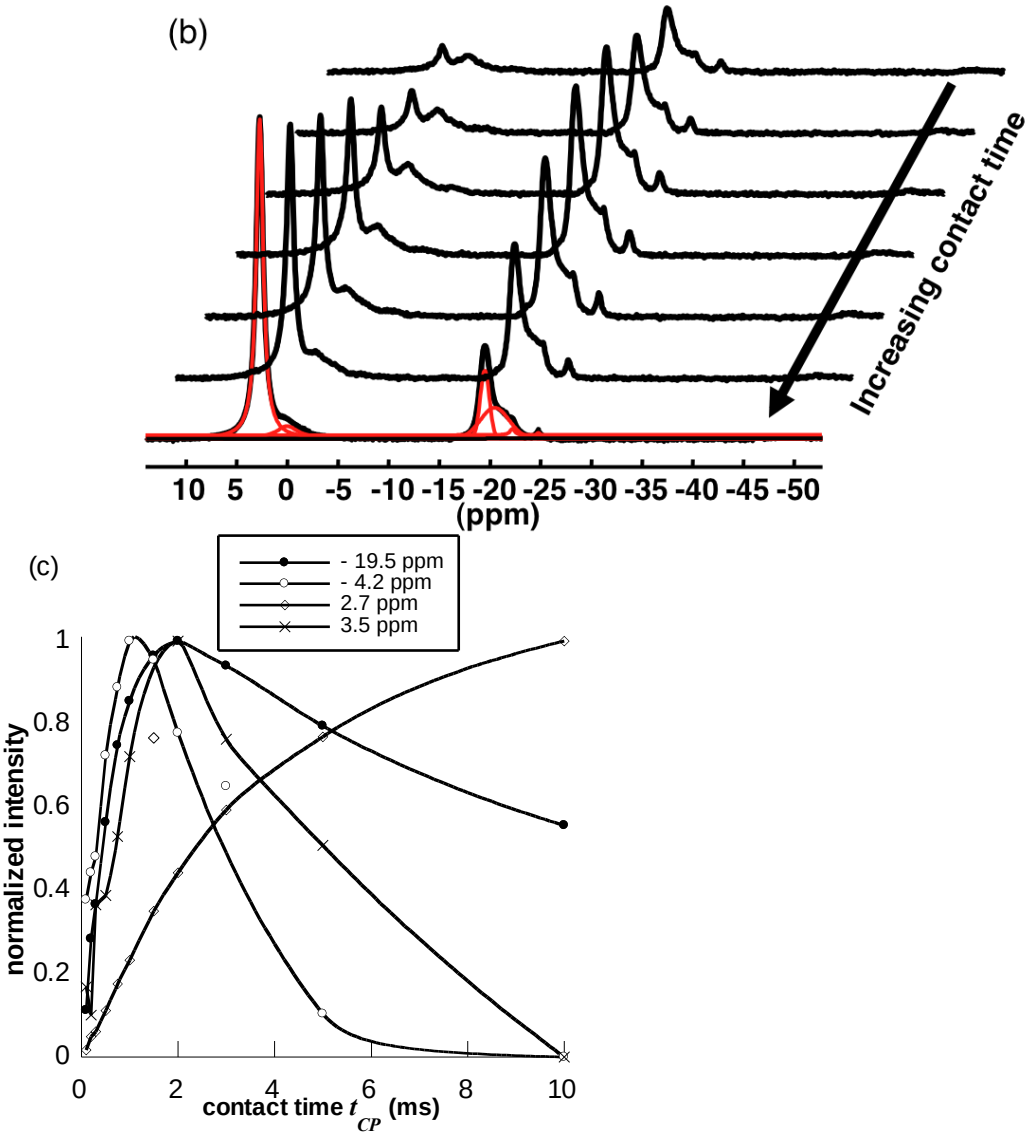

Figure 4. (a) $\{^1H\}$-^{31}P HPDec MAS spectra of HAp (with red lines indicating deconvolution) and nanocomposites, (b) selected $\{^1H\}$-^{31}P CP MAS spectra of *ZH4* as a function of contact time t_{CP} from 0.1 ms (top line) to 10 ms (bottom line, with red lines indicating deconvolution) and (c) evolution of the

normalized intensity of selected signals as a function of t_{CP} as obtained from (b). Titled x-axis for (a) and (b) and plain lines on (c) are for eye guidance only.

The results obtained from the NMR data suggested that the apatite structure was well-preserved within the nanocomposite materials. It was also important to identify any effect of the presence of apatite on the zirconia phase. With this purpose, selected samples were heated up to 900°C and studied by XRD (Figure 5). For the apatite sample, peak narrowing is observed and no other calcium phosphate phase differing from HAp (JCPDS 09-0432) is appearing. For the pure ZrO_2, all peaks can be attributed to the monoclinic *m*-ZrO_2 phase are apparent (JCPDS 37-1484). In contrast, for *ZH1* materials, main diffractions peaks belong to the tetragonal *t*-ZrO_2 phase (JCPDS-17-0923), although the presence of *m*-ZrO_2 in small amounts cannot be put aside due to possible overlap with peaks of the HAp phase. Noticeably, no diffraction peak corresponding to zirconium phosphate phases could be identified. Moreover, the formation of *t*-ZrO_2 is in agreement with previous reports showing that phosphate ions could influence the crystallization of ZrO_2 from zirconium hydroxide.[60] Coming back to our previous hypothesis based on NMR data, these experiments suggest that released phosphates are incorporated within the growing ZrO_2 colloids during the sol-gel reaction.

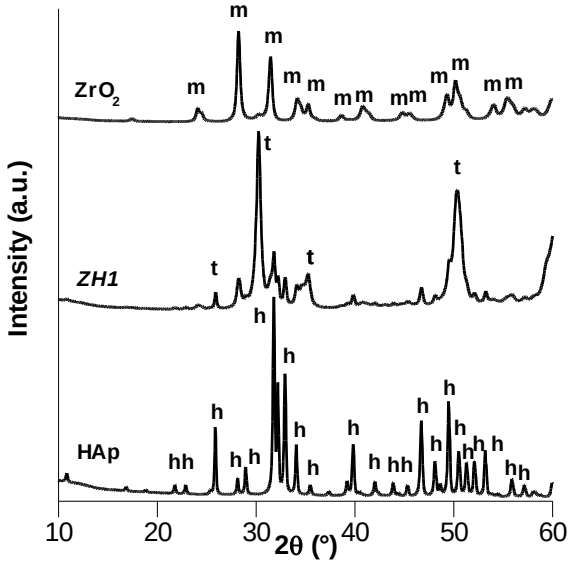

Figure 5. XRD diffractograms of HAp, *ZH1* and ZrO_2 after thermal treatment at 900°C. h, t and m corresponds to diffraction peaks from hydroxyapatite, *t*-ZrO_2 and *m*-ZrO_2, respectively, as obtained from corresponding JCPDS files.

3.3. Metal ion sorption experiments. To investigate in details the surface properties of composite phases, three species were selected, Pb(II), Cr(III) and $Cr_2(VI)O_7^{2-}$ not only due to their environmental relevance[51] but to evaluate their relative affinities towards apatite and zirconia. Indeed, apatites are well-known adsorbents of metal cations.[17] This is due to a combination of high affinity of surface phosphate groups for cations, possible exchange with calcium ions and precipitation of metal phosphate as a result of the surface dissolution of apatite.[11,17] In parallel, studies devoted to metal cations sorption on hydrated zirconia showed that the binding process mainly involved hydroxyl groups of the inorganic phase.[61] For inorganic anions, binding to Ca(II) and Zr(IV) centers could be expected.

In a first step, the adsorption of Pb(II) ions was studied. Sorption isotherms are shown on Figure 6, indicating that the maximum loading decreases with apatite content from 330 $mg.g^{-1}$ for HAp down to 50 $mg.g^{-1}$ for ZrO_2. The fact such a decrease varies inversely with S_{BET} confirms that the apatite content is the key factor determining the sorption capacity. It is also worth noting that *ZH0.25* has a maximum capacity twice lower than pure apatite despite the fact that it contains only 20 % ZrO_2. Attempts were made to fit the experimental data with Langmuir model. For the pure *HAP* and *ZH0.25*, the experimental capacity could be suitably reproduced but low R^2 values (0.96) were obtained. For *ZH4*, a suitable fitting of the experimental data (R^2 = 0.998) was achieved. For pure ZrO_2, the Langmuir model was not adapted (R^2 = 0.832). Parameters obtained from selected simulations are gathered in Table 2 and corresponding curves are shown on Fig. 7. These results can be understood taking into account (1) the well-known precipitation of hydroxypyromorphite $Pb_{10}(PO_4)_6(OH)_2$ at the surface of apatite,[62] and (2) the low acidity of Pb^{2+} therefore presenting limited affinity for the hydroxyl groups of the Zr-phase.

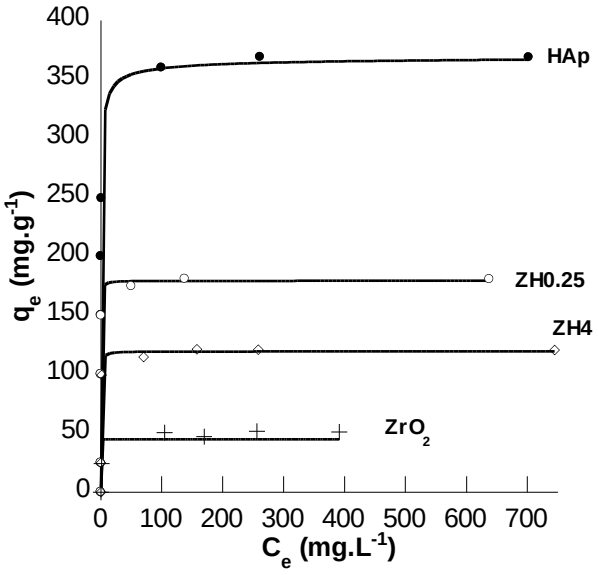

Figure 6. Pb^{2+} sorption isotherms on selected materials. Plain lines correspond to the simulation of experimental data using the Langmuir model.

The opposite trend was observed for $Cr_2(VI)O_7^{2-}$, with the highest sorption capacity being achieved for ZrO_2 (*ca*. 110 mg.g^{-1}) and lowest capacity for pure *HAp* (ca. 18 mg.g^{-1}) (Figure 7) . All data are well-fitted by the Langmuir equation ($R^2 > 0.98$) (Table 2 and Fig. 7). It must be pointed out that the sorption capacity does not seem to depend directly on the specific surface area as a minor increase in sorption capacity, from 18 mg.g^{-1} to 27 mg.g^{-1}, is observed from *HAp* to *ZH0.25* despite an increase in S_{BET} from *ca*. 100 m^2.g^{-1} to 200 m^2.g^{-1}. Therefore, our data reflect the low affinity of apatite for $Cr_2(VI)O_7^{2-}$ due to electrostatic repulsion with the phosphate and hydroxyl groups and the attractive electrostatic interaction between ZrO_2 and polyanions.[63]

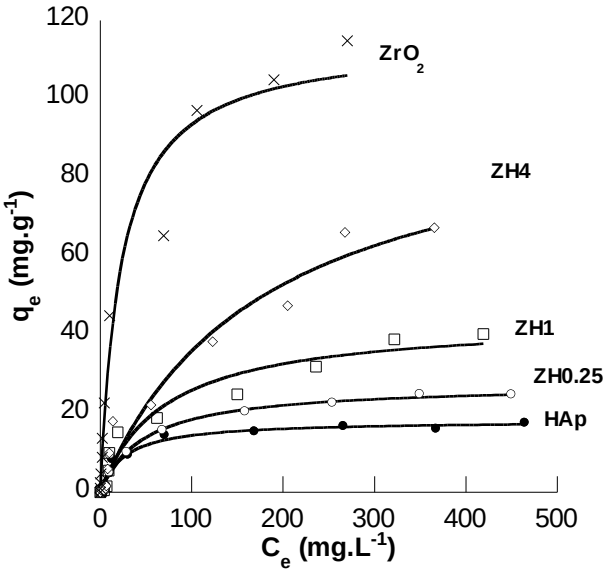

Figure 7. $Cr_2O_7^{2-}$ sorption isotherms on pure phases and nanocomposites. Plain lines correspond to the simulation of experimental data using the Langmuir model.

The sorption of Cr^{3+} followed a trend similar to Pb^{2+} in terms of maximum capacity that decreases with decreasing apatite content of the samples (Figure 8). As mentioned earlier, such variations are not directly related to the specific area of the sorbent, as a calculations of maximum capacity per surface unit indicate values of 0.04 mg.m^{-2}, 0.20 mg.m^{-2}, 0.30 mg.m^{-2}, 0.40 mg.m^{-2} and 2.55 mg.m^{-2} for ZrO_2, *ZH4*, *ZH1*, *ZH0.25* and HAp, respectively. However, a first observation is that for ZrO_2 the maximum capacity is lower than Pb^{2+} in weight content (*ca*. 15 mg.g^{-1} compared to *ca*. 60 mg.g^{-1}) but similar in mole content (0.29 mmole.g^{-1} value). Similar calculations indicate a higher molar content of Cr^{3+} compared to Pb^{2+} for *ZH4* (1.25 mmole.g^{-1} vs 0.57 mmole.g^{-1}) and *ZH0.25* (1.75 mmole.g^{-1} vs 0.85 mmole.g^{-1}). This calculation cannot be performed for pure HAp because a maximum could not be reached for initial Cr^{3+} concentration of 500 mg.L^{-1}. Langmuir equation showed reasonable fitting parameters with a strong variation of *K* with the *ZrO_2:HAp* ratio. Our data can be interpreted as the result of the high affinity of HAp for Cr^{3+}, as previously suggested in the literature,[64] and more limited sorption of this cation on ZrO_2. Note that attempts made to use chromium solutions at higher concentrations (*i.e.* 1 g.L^{-1}) led to poorly reproducible data, that may originate from the increase of pH

usually observed during metal adsorption on apatite,[65] that may have led to the precipitation of chromium hydroxide phases.

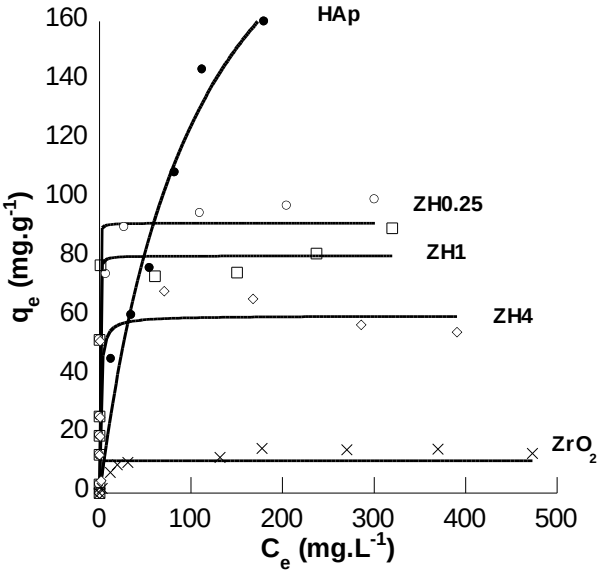

Figure 8. Cr^{3+} sorption isotherms on pure phases and nanocomposites. Plain lines correspond to the simulation of experimental data using the Langmuir model.

Table 2. Maximum capacity ($q_{e,max}$) and Langmuir constant (K) obtained from the modeling of the metal sorption isotherms using Langmuir equation. R^2 correspond to the correlation coefficient as obtained from non-linear fitting

	Pb^{2+}			$Cr_2O_7^{2-}$			Cr^{3+}		
	$q_{e,max}$ ($mg.g^{-1}$)	K	R^2	$q_{e,max}$ ($mg.g^{-1}$)	K	R^2	$q_{e,max}$ ($mg.g^{-1}$)	K	R^2
ZrO_2	50	-[a]	0.832	115	0.04	0.984	10	-[a]	0.645
ZH4	120	4	0.998	100	0.04	0.983	60	0.1	0.831
ZH1	nd	nd	nd	45	0.02	0.987	80	10	0.925
ZH0.25	175	8	0.965	25	0.02	0.985	90	15	0.987
HAp	335	8	0.962	15	0.02	0.986	260	0.01	0.972

[a] non significant value; nd = not determined

It is worth noting that the overall accurate fitting of sorption data by the Langmuir model for the three metal ions is rather surprising as this model is adapted to homogeneous surfaces. Attempts were made to use a Freundlich-type model that is usually applied for sorption data on heterogeneous surfaces.[66] However, in most cases, corresponding curves hardly fitted experimental data (see SI-8) and extracted parameters were often non significant, although we do not have a clear explanation for this at this time.

The strength of the metal-composite interactions was also studied via desorption experiments. Because sorption data were obtained in acidic conditions, and based on the literature,[67] desorption was performed in alkaline conditions, *i.e*. pH 9 and 11. However, in these conditions, Cr^{3+} species precipitate as $Cr(OH)_3$ so that only low recovery rate (2 % <) were obtained. In the case of Cr(VI) species, the desorption rate increases from pH 9 to pH 11 and, at fixed pH, from HAp to ZrO_2 with intermediate values for *ZH1* (Figure 9a). Taking into account that the point of zero charge (pzc) of zirconia lies in the 6-7 pH range, the easy recovery from ZrO_2 phase can be understood on the basis of the change of surface charge from positive in the acidic conditions of sorption to negative in alkaline condition, resulting in repulsive electrostatic interactions with the anionic Cr(VI) species. In the case of HAp, the desorption rate was low (5-10 %), suggesting strong interactions with the apatite phase. The most plausible explanation is that CrO_4^{2-} species, that are the main form of Cr(VI) species at low concentration and high pH, can substitute PO_4^{2-} ions in the apatite structure, as previously demonstrated.[68]

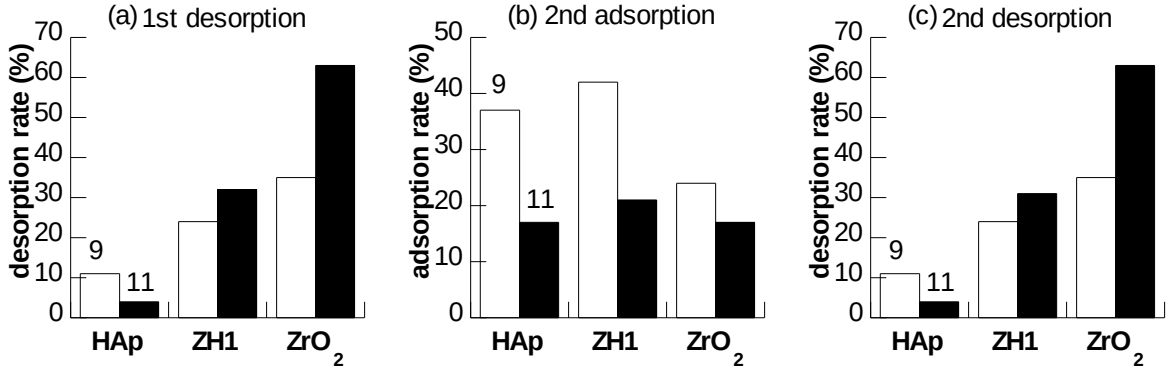

Figure 9. Recycling of HAp, *ZH1* and ZrO_2 materials as sorbents for Cr(VI) species: (a) first desorption rate, (b) second adsorption rate and (c) second desorption rate. Desorption was made at pH 9 (white) and pH 11 (dark).

To investigate further these phenomena, an additional adsorption/desorption cycle was performed. Despite their lower initial desorption rate, materials treated at pH 9 showed better preservation of sorption capacity (25-40 % compared to initial sorption capacity) compared to those treated at pH 11 (Fig. 9b). In these conditions, HAp and *ZH1* show sorption capacities higher than desorption rates, suggesting that the alkaline treatment enhances the affinity of the apatite phase for Cr(VI) species. The opposite situation is observed for ZrO_2. The fact that these trends are even more pronounced at pH 11 confirms that they are mainly related to the alkaline conditions. Another indication is provided by the results of a second desorption step that shows similar Cr(VI) release values compared to the first desorption experiments (Fig. 9c). This suggests irreversible modifications of the material surface reactivity after the first alkaline treatment. Although apatite is known to be stable in alkaline conditions, high pH favors the carbonatation of the apatitic structure,[69] resulting in a shift of the pZc of apatite towards more basic pH,[70] that should favor the electrostatic adsorption of anionic Cr(VI) species in acidic conditions. Zirconia is also known to be very stable in basic media but, considering the conditions of the sol-gel procedure, it can be suggested that the alkaline treatment enhances the condensation state of the hydrated zirconium oxide particles, therefore decreasing the number of surface Zr-OH groups available for adsorption of Cr(IV) anionic species.

In the context of metal ion depollution, these data indicate that pure HAp is the most favorable if Pb^{2+} and/or Cr^{3+} are present whereas ZrO_2 is more adapted if $Cr_2O_7^{2-}$ is present. However, in case of Pb(II)/Cr(VI) or Cr(III)/Cr(VI) mixtures, nanocomposites can be advantageous, especially the *ZH4* (i.e. higher ZrO_2 content) material that combines a high specific surface area with good affinity for Cr(VI) while maintaining Pb(II) and Cr(III) maximum capacities that do not differ too importantly from *ZH0.25* (i.e. higher HAp content). Note that the presence of phosphate groups associated with the zirconia phase,

as indicated by NMR and XRD data, may contribute to the affinity of *ZH4* for metal cations. Such an affinity for both Cr^{3+} and $Cr_2O_7^{2-}$ is of large interest because, in remediation processes, the highly toxic Cr(VI) ions are often converted via oxidation reaction into less detrimental Cr(III) ions.[49,71,72] It is therefore advantageous that the sorbent phase exhibits a combined affinity for both species to avoid release of Cr^{3+} after conversion. In addition, our adsorption/desorption experiments also indicate that nanocomposites *ZH1* represent an interesting compromise in terms of recyclability for Cr(VI) species.

4. CONCLUSIONS

It was possible to prepare zirconia-hydroxyapatite nanocomposites by taking into account the various constraints inherent to this biphasic system, such as colloidal dispersion of HAp nanoparticles and pH conditions compatible with both ZrO_2 gel formation and HAp stability. In particular, it was possible to avoid the formation of calcium zirconate phase often reported in the literature. Zirconium phosphate phases were apparently not precipitated during the process but Zr-O-P bonds could be evidenced, leading to the stabilization of the *t*-ZrO_2 phase upon heating. Resulting materials, obtained by soft chemistry approaches, show very promising properties in terms of surface affinity for both cationic and anionic metallic species. Their dual porosity in the microporous and mesoporous range may also be of significant interest in the field of biomaterials. In parallel, it should be possible to substitute the zirconium alkoxide by a wide range of alternative sol-gel precursors, opening the route to the design of a novel class of apatite-based nanocomposites.

Acknowledgments. We wish to thank Dr T. Azaïs and Dr C. Coelho (LCMCP) for their assistance in NMR experiments.

Supporting Information Available. DLS studies of the stability of apatite colloids, complete sets of SEM images, TEM images and N_2-sorption curves, porous volume and pore diameter from the Innes model, deconvoluted $\{^1H\}$-^{31}P CP MAS spectra of *ZH4* at 2 ms contact time and evolution of the

normalized intensity of selected signals as a function of contact time, sorption data fitting using a Freundlich-type model. This material is available free of charge via the Internet at http://pubs.acs.org.

REFERENCES

1. LeGeros, R. Z. *Calcium Phosphates in Oral Biology and Medicine. Monographs in Oral Sciences*; Myers, H., Ed.; Karger: Basel, **1991**; Vol. 15.
2. Ellliott, J. C. *Structure and Chemistry of Apatites and other Calcium Orthophosphates*; Elsevier: The Netherlands, **1994**.
3. Dorozhkin, S. V. *Materials* **2009**, *2*, 399-498
4. Al Kattan, A. ; Errassifi, F. ; Sautereau, A. M. ; Sarda, S. ; Dufour, P. ; Darroug, A. ; Dos Santos, I. ; Combes, C. ; Grossin, D. ; Rey, C. ; Drouet, C. *Adv. Engin. Mater.* **2010**, *12*, B224-B233
5. Isobe, T. ; Nakamura, S. ; Nemoto, R. ; Senna, M. ; Sfihi, H. *J. Phys. Chem. B*, 2002, *16*, 5169-5176
6. Jäger, C. ; Welzel, T. ; Meyer-Zaika, W. ; Epple, M. *Magn. Res. Chem*. 2006, *44*, 573-580.
7. Tseng, Y.-H. ; Tsai, Y.-L. ; Tsai, W. T. ; Chao, J. C. H. ; Lin, C.-P. ; Huang, S.-H.; Mou, C. Y. ; Chan, J. C. C. *Chem. Mater*. 2007, *19*, 6088-6094.
8. Bertinetti, L. ; Tampieri, A. ; Landi, E. ; Ducati, C. ; Midgley, P. A. ; Coluccia, S. ; Martra, G. *J. Phys. Chem. C* **2007**, *111*, 4027-4035.
9. Huang, S.-J.; Tsai, Y.-L.; Lee, Y.-L.; Lin, C. -P.; Chan, J. C. C. *Chem. Mater*. **2009**, *21*, 2583–2585
10. Nassif, N. ; Martineau, F. ; Syzgantseva, O. ; Gobeaux, F. ; Willinger, M. ; Coradin, T. ; Cassaignon, S. ; Azaïs, T. ; Giraud-Guille, M. M. *Chem. Mater*. **2010**, *22*, 3653-3663.
11. Rey, C. ; Combes, C. ; Drouet, C. ; Sifhi, H. ; Barroug, A. *Mater. Sci. Engin. C* **2007**, *27*, 198-205
12. Sakhno, Y. ; Bertinetti, L. ; Iafisco, M. ; Tampieri, A. ; Roveri, N. ; Martra, G. *J. Phys. Chem. C* **2010**, *114*, 16640-16648

13. Vyalikh, A. ; Simon, P. ; Kollmann, T. ; Kniep, R. ; Scheler, U. *J. Phys. Chem. C* **2011**, *115*, 1513-1519

14. Dahl, S. G. ; Allain, P. ; Marie, P. J. ; Mauras, Y. ; Boivin, G. ; Ammann, P. ; Tsouderos, Y. ; Delmas, P. D. ; Christiansen, C. *Bone* **2001**, *28*, 446-453.

15. Dowd, T. L. ; Rosen, J. F. ; Mints, L. ; Gundberg, C. M. *Biochim. Biophys. Acta – Mol. Basis Disease* **2001**, *1535*, 153-163.

16. Cazalbou, S. ; Eichert, D. ; Drouet, C. ; Combes, C. ; Rey, C. *C.R. Palevol* **2004**, *3*, 563-572

17. Valsami-Jones, E. ; Ragnarsdottir. K.V. ; Putnis, A. ; Bosbach, D.; Kemp, A.J. ; Cressey, G. *Chem. Geol*. **1998**, *151*, 215-233.

18. Dybowska, A. ; Manning, D. A. C. ; Collins, M. J. ; Wess, T. ; Woodgate, S. ; Valsami-Jones, E., *Sci. Tot. Environ*. **2009**, *407*, 2953–2965

19. *Bioceramics and their clinical applications*; Kokubo, T., Ed.; Woodhead Publishing Ltd: Cambridge, **2008**

20. Andersson, J. ; Areva, S. ; Spliethoff, B. ; Linden, M. *Biomaterials* **2005**, *26*, 6827–6835.

21. Li, X.W. ; Yasuda, H.Y. ; Umakoshi, Y. *J. Mater. Sci. : Mater. Med*. **2006**, *17*, 573-581.

22. Chang, J.H. ; Park, M.E. ; Shin, Y. ; Exarhos, G.J. ; Kim, K.J. ; Lee, S.C. ; Oh, K.S. *J. Mater. Chem*. **2007**, *17*, 238-242.

23. Li, J. ; Fartash, B. ; Hermansson, L. *Biomaterials* **1995**, *16*, 417-422.

24. Kim, S. ; Kong, Y.-M. ; Lee, I.-S. ; Kim, H.-E. *J. Mater. Sci. Mater Med*. **2002**, *13*, 307-310.

25. Viswanath, B. ; Ravishankar, N. *Scripta Mater*. **2006**, *55*, 863-866.

26. Ramires, P.A. ; Wennernerg, A. ; Johansson, C.B. ; Cosentino, F. ; Tundo, S. ; Milella, E. *J. Mater. Sci. Mater. Med*. **2003**, *14*, 539-545.

27. Pushpakanth, S. ; Srinavasan, B. ; Sreedhar, B. ; Sastry, T.P. *Mater. Chem. Phys*. **2008**, *107*, 492-498.

28. Nayak, S. ; Satpati, B. ; Shukla, R.K. ; Dhawan, A. ; Bhattacherjee, S. ; Chaudhary, Y.S. *J. Mater. Chem.* **2010**, *20*, 4949-4954.

29. Adolfsson, E., Alberius-Henning, P. ; Hermansson, L. *J. Am. Ceram. Soc*. **2000**, *83*, 2798–2802

30. Rao R.R. ; Kannan, T.S. *Mater. Sci. Engin. C* **2002**, *20*, 187-193.

31. Evis, Z. ; Usta, M. ; Kutbay, I. *J. Eur. Ceram. Soc*. **2009**, *29*, 621-628

32. Nakahira, A. ; Okajima, T. ; Honma, T. ; Yoshioka, S. ; Tanak, I. *Chem. Lett*. **2006**, *35*, 856-857.

33. Nathanael, A. J. ; Mangalaraj, D. ; Chen, P.C. ; Ponpandian, N. *Composite Sci. Technol*. **2010**, *70*, 419-426.

34. Sheng, G. ; Qiao, L. ; Mou, Y. J. *Environ. Engin.- ASCE* **2011**, *137*, 611-616.

35. Suchanek, W.J. ; Riman, R.E. *Adv. Sci. Technol*. **2006**, 45, 184-193.

36. Chiu, C.-Y. ; Hsu, H.-C. ; Tuan, W.-H. *Ceram. Int*. **2007**, *33*, 715-718

37. Li, W. ; Gao, L. *Biomaterials*, **2003**, *24*, 937–940.

38. Xu, J.L. ; Khor, K.A. *J. Inorg. Biochem*. **2007**, *101*, 187-195.

39. Texeira Da Costa, P. ; Ogasawara, T. ; De Souza Nobreiga, M.C. ; Fernandes Lourenço Gomes, L.C. *J. Sol-Gel Sci. Technol*. **1998**, *13*, 251-254.

40. Katam, S. ; Rama Krishna, D.S. ; Murugan, R. ; Sampath Kumar, T.S. *Trends Biomater. Artif. Organs* **2003**, *17*, 24-27.

41. Wu, J.-M. ; Yeh, T.-S. *J. Mater. Sci*. **1988**, *23*, 3771-3777.

42. Liu, Y. ; Nancollas, G.H. *J. Phys. Chem. B* **1997**, *101*, 3464-3468.

43. Uota, M. ; Arakawa, H. ; Kitamura, N. ; Yoshimura, T. ; Tanaka, J. ; Kijima, T. *Langmuir* **2005**, *21*, 4724–4728

44. Andres, C. ; Sinani, V. ; Lee, D. ; Gun'ko, Y. ; Kotov, N. *J. Mater. Chem*. **2006**, *16*, 3964-3968.

45. Bouladjine, A. ; Al-Kattan, A. ; Dufour, P. Drouet, C. *Langmuir* **2009**, *25*, 12256-12265

46. Piconi, C. ; Maccauro, G. *Biomaterials* **1999**, *20*, 1-25.

47. Ahn, E. S. ; Gleason, N. J. ; Nakahira, A. ; Ying, J. Y. *Nano Lett*. **2001**, 1, 149-153

48. Anh, E. S ; Gleason, N. J. ; Ying, J. Y. *J. Am. Ceram. Soc*. **2005**, *88*, 3374-3379

49. Fu, F. ; Wang, Q. J. *Environ. Manag*. **2011**, *92*, 407-418.

50. El-Hammari, L. ; Merroun, H. ; Coradin, T. ; Cassaignon, S. ; Laghzizil, A. ; Saoiabi, A. *Mater.*

Chem. Phys. **2007**, *104*, 448–453

51. Bokhimi, X. ; Morales, A. ; Novaro, O. ; Portilla, M. ; Lopez, T. ; Tzompantzl, F. ; Gomez, R. *J. Solid State Chem*. **1998**, *135*, 28-35
52. Thornton, I. ; Butler, D. ; Docx, P. ; Hession, M. ; Makropolous, C. ; McMullen, M. ; Nieuwenhuijsen, M. ; Pitman, A. ; Rautiu, R. ; Sawyer, R. ; Smith, S. ; White, D. ; Wilderer, P. ; Paris, S. ; Marani, D. ; Braguglia, C. ; Palerm, J. *Pollutants in urban waste water and sewage sludge* ; European Communities : Luxembourg, **2001.**
53. Pang, G. ; Sominska, E. ; Cölfen, H. ; Mastai, Y. ; Avivi, S. ; Koltypin, Y. ; Gedanken, A. *Langmuir* **2001**, *17*, 3223-3226.
54. Gao, Y. ; Masuda, Y. ; Ohta, H. ; Koumoto, K. *Chem. Mater*. **2004**, *16*, 2615-2622.
55. Rouquerol, J. ; Avnir, D. ; Fairbridge, C. W. ; Everett, D. H. ; Hayner, J. M. ; Pernicone, N. ; Ramsay, J. D. F. ; Singh, K. S. W. ; Unger, K. K. *Pure Appl. Chem*. **1994**, *66*, 1739-1758.
56. Innes, W. B. *Anal. Chem*. **1957**, *29*, 1069-1073.
57. Clayden, N. J. *J. Chem. Soc. Dalton Trans*. **1987**, 1877-1881
58. Alfaya, A. A. S. ; Gushikem, Y. ; de Santos, S. C. *Microporous Mesoporous Mater*. **2000**, *39*, 57-65
59. Yan, Z. ; Kirby, C. W. ; Huang, Y. *J. Phys. Chem. C* **2008**, *112*, 8575-8586
60. Mekhemer, G. A. H. *Colloids Surf A* **1998**, *141*, 227-235
61. Sakellaridis, P. U. ; Nobelis, F. Z. *J. Inorg. Nucl. Chem*. **1974**, *36*, 2599-2603.
62. Peld, M. ; Tonsuaadu, K. ; Bender, V. *Environ. Sci. Technol*. **2004**, *38*, 5626–5631.
63. Chen, F. R. ; Coudurier, G. ; Joly, J. F. ; Vedrine, J. C. *J. Catal*. **1993**, *143*, 616-626.
64. Peld, M. ; Tonsuaadu, K. ; Bender, V. *Proc. Estonian Acad. Sci. Chem*. **2004**, *53*, 75-90
65. El Asri, S. ; Laghzizil, A. ; Coradin, T. ; Saoiabi, A. ; Alaoui, A. ; M'hamedi, R. *Colloids Surf. A* **2010**, *362*, 33-38
66. Otake, Y. ; Kalili, N. ; Chang, T. H. ; Furuya, E. *Separ. Purif. Technol*. **2004**, *39*, 67-72.
67. Selvi, K. ; Pattabhi, S. ; Kadirvelu, K. *Biores. Technol*. **2001**, *80*, 87-89.

68. Hummel, F. A. ; Grisafe, D. A. *J. Solid State Chem*. **1970**, *2*, 160-166.

69. Simpson, D. R. *Am. Miner*. **1967**, *52*, 896-902.

70. Landi, E. ; Celotti, G. ; Logroscino, G. ; Tampieri, A. *J. Eur. Ceram. Soc*. **2003**, *23*, 2931-2937.

71. Palmer, C. D. ; Wittbrodt, P. R. *Env. Health. Persp*. **1991**, *92*, 25-40

72. Mohan, D. ; Pittman Jr., C. U. *J. Hazard. Mater*. **2006**, *137*, 762-811

Synopsis graphic

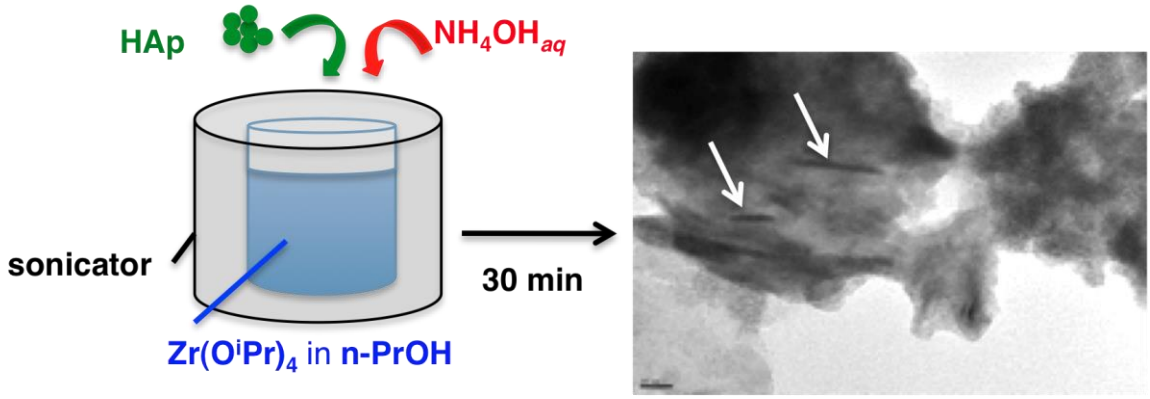

Ultrasound-assisted synthesis of mesoporous zirconia-hydroxyapatite nanocomposites and their mixed surface affinity for $Cr^{3+}/Cr_2O_7^{2-}$ ions

Karima Achelhi,[¥,‡] Sylvie Masse,[¥] Guillaume Laurent,[¥] Abdelaziz Laghzizil,[‡] Ahmed Saoiabi,[‡] and Thibaud Coradin[¥,]*

SUPPLEMENTARY INFORMATION

(a) (b)

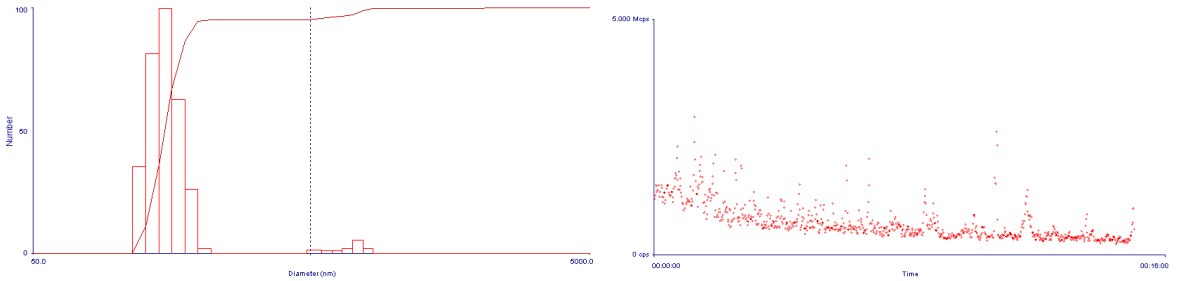

(c) (d)

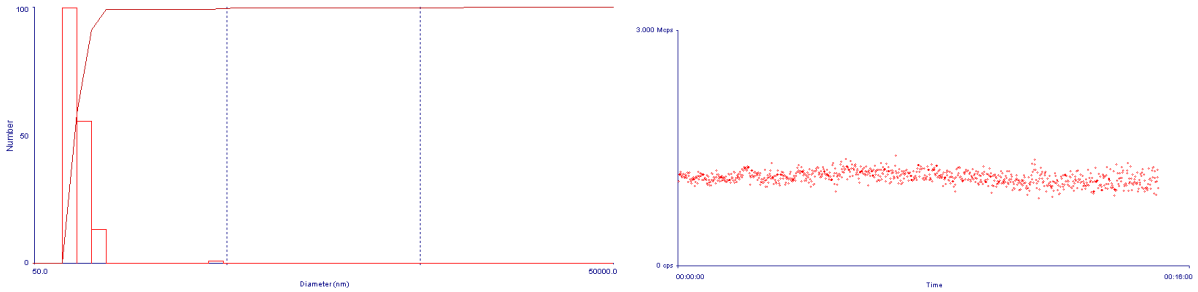

(e) (f)

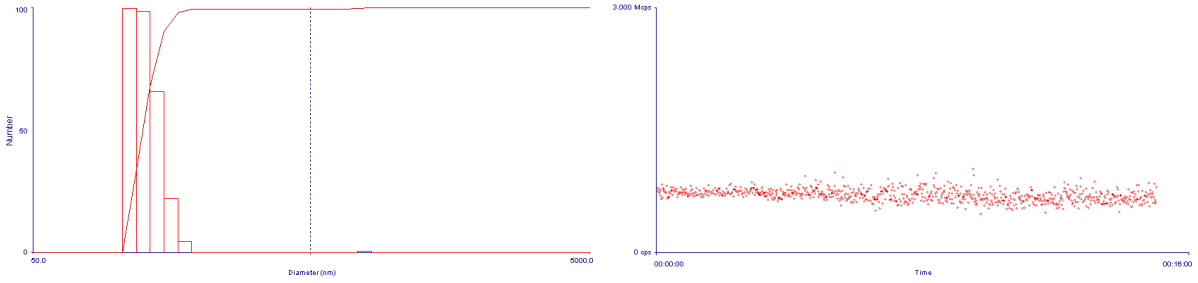

SI-1. DLS studies of apatite suspension (left hand column, particle size distribution after 30 min utrasonication; right hand column : intensity variation) for (a,b) 0.5 mg.mL^{-1} suspension in 1-propanol, (c,d) 0.25 mg.mL^{-1} suspension in 1-propanol and (d,e) 0.25 mg.mL-1 suspension in the alkoxide solution

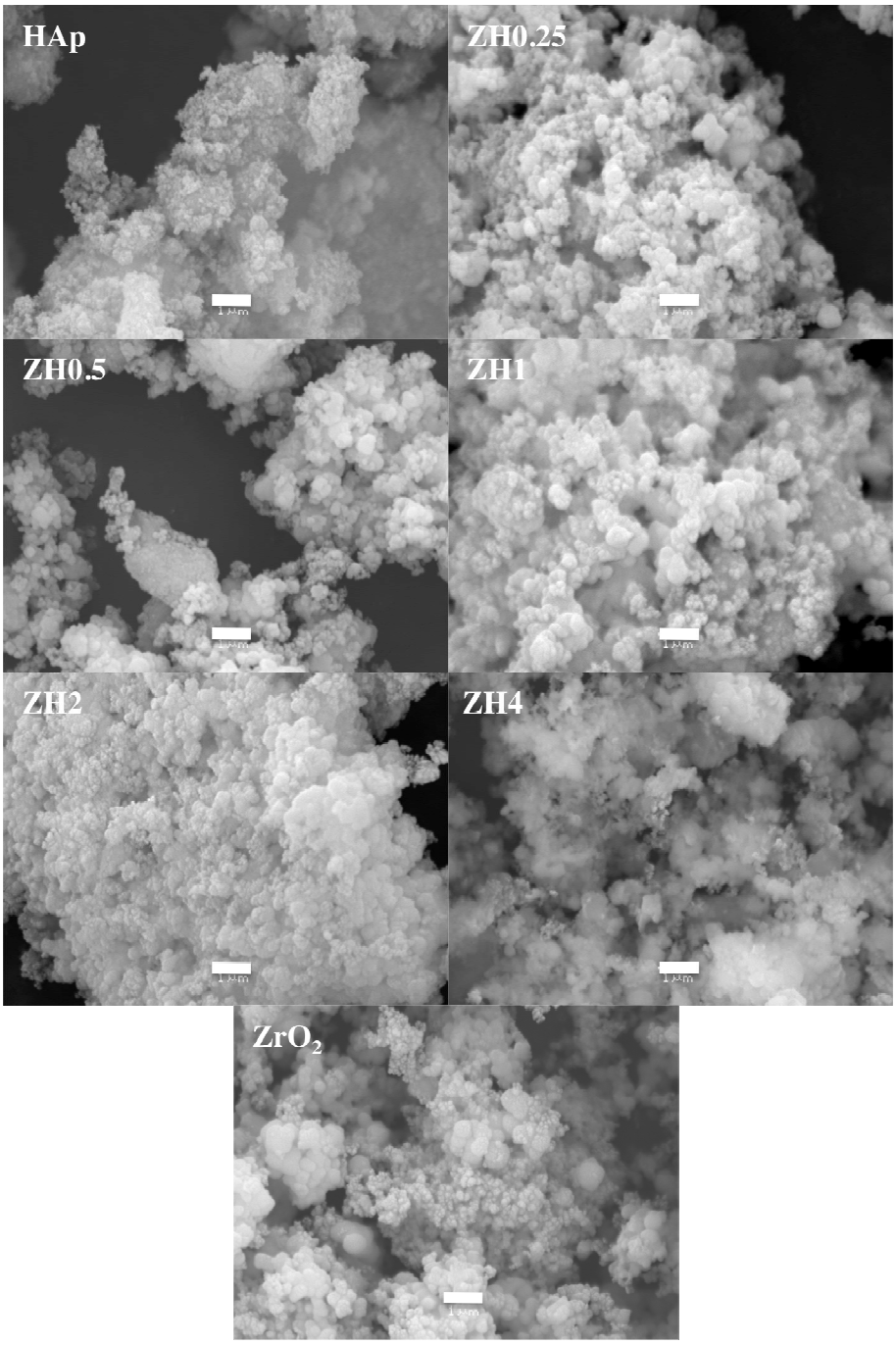

SI-2. SEM images for all samples (scale bar = 1 μm)

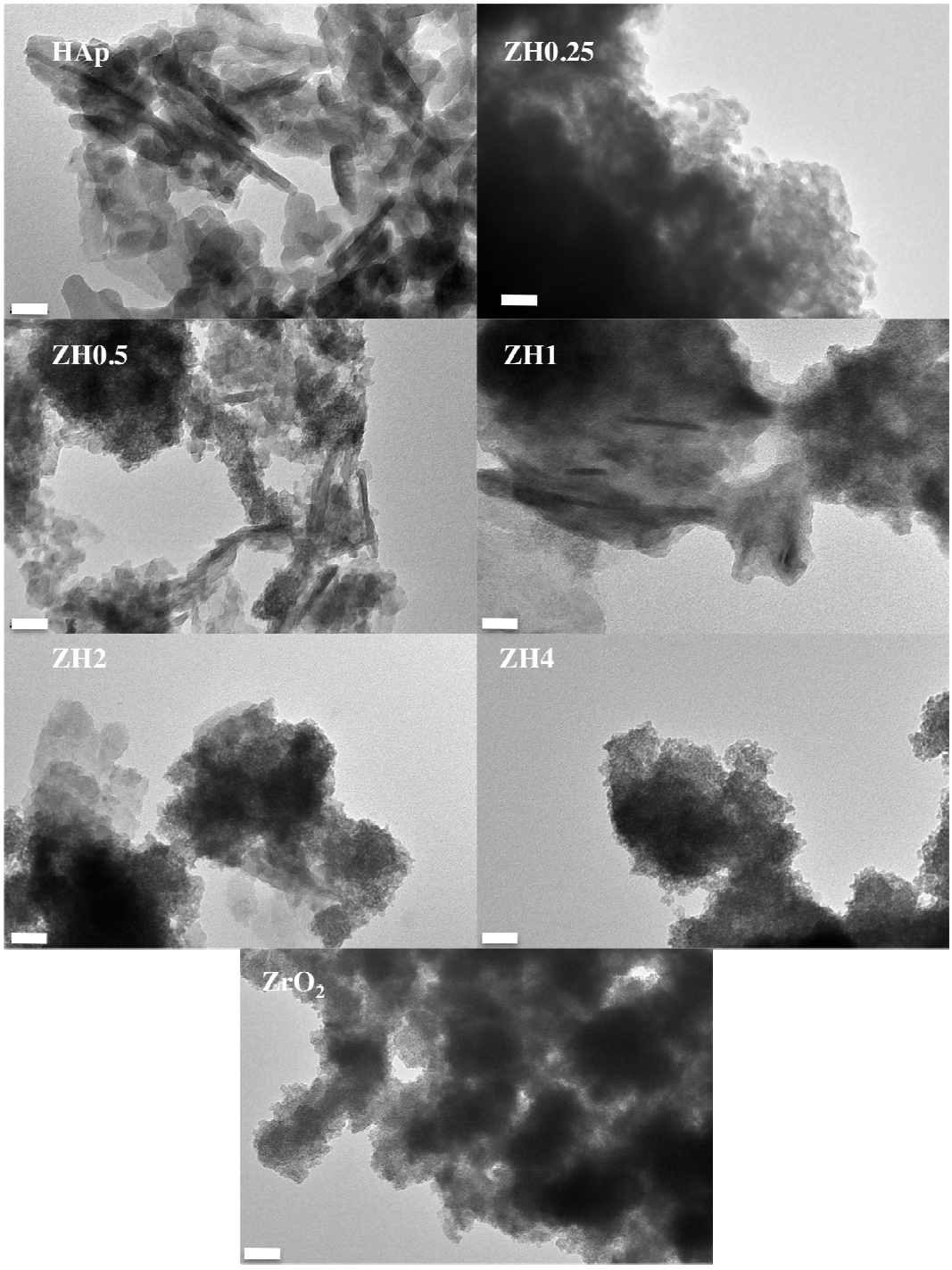

SI-3. TEM images for all samples (scale bar = 20 nm)

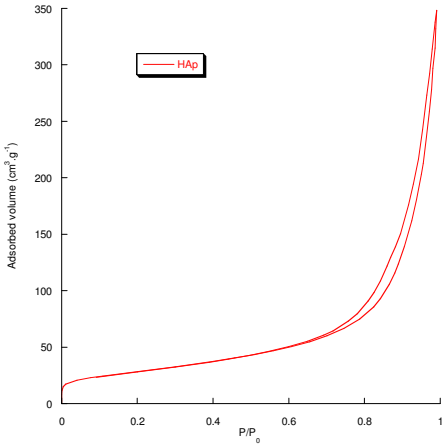
HAp
Adsorbed volume (cm3.g-1)
P/P0
0
50
100
150
200
250
300
350
0.2
0.4
0.6
0.8
1

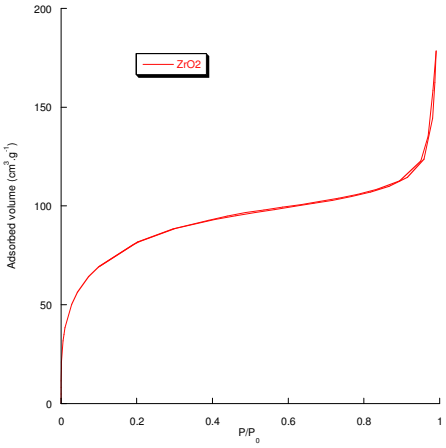
ZrO2
Adsorbed volume (cm3.g-1)
P/P0
0
50
100
150
200
0.2
0.4
0.6
0.8
1

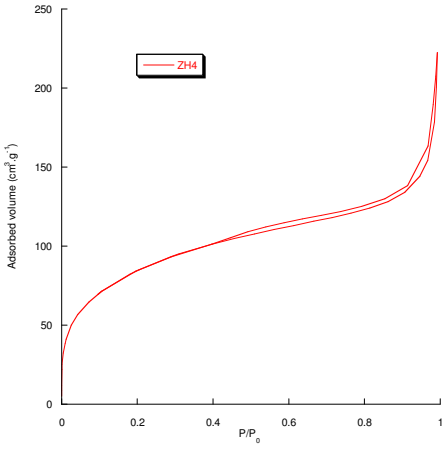
ZH4
Adsorbed volume (cm3.g-1)
P/P0
0
50
100
150
200
250
0.2
0.4
0.6
0.8
1

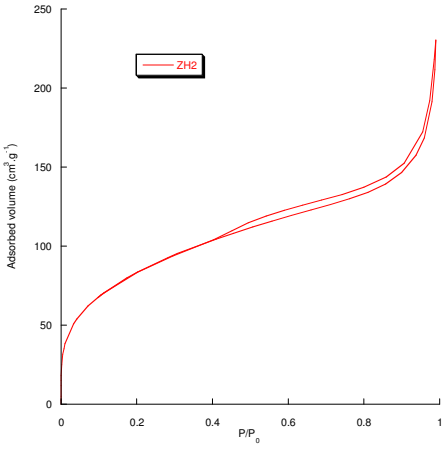
ZH2
Adsorbed volume (cm3.g-1)
P/P0
0
50
100
150
200
250
0.2
0.4
0.6
0.8
1

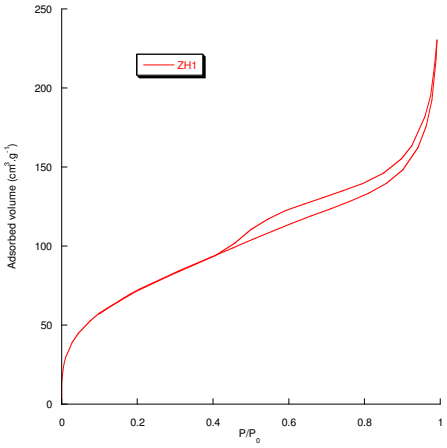
ZH1
Adsorbed volume (cm3.g-1)
P/P0
0
50
100
150
200
250
0.2
0.4
0.6
0.8
1

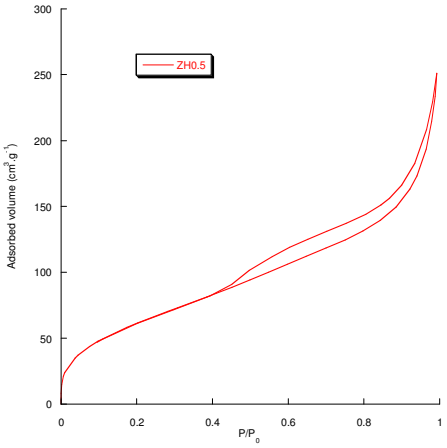
ZH0.5
Adsorbed volume (cm3.g-1)
P/P0
0
50
100
150
200
250
300
0.2
0.4
0.6
0.8
1

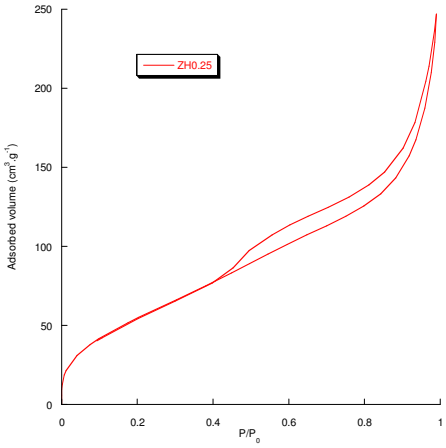

SI-4. Individual N_2-sorption isotherms for all samples

Table SI-5. Porous volume (V_p) and average pore size (D_p) from Innes[1] model of pure phases (ZrO_2, HAp) and nanocomposites

Sample	V_p ($cm^3.g^{-1}$)	D_p (nm)
ZrO_2	0.18	1.6
ZH4	0.25	1.6
ZH2	0.29	1.6
ZH1	0.30	1.7
ZH0.5	0.34	1.7
ZH0.25	0.36	2.1
HAp	0.53	8.0

1. Innes, W. B. *Anal. Chem*. **1957**, *29*, 1069-1073.

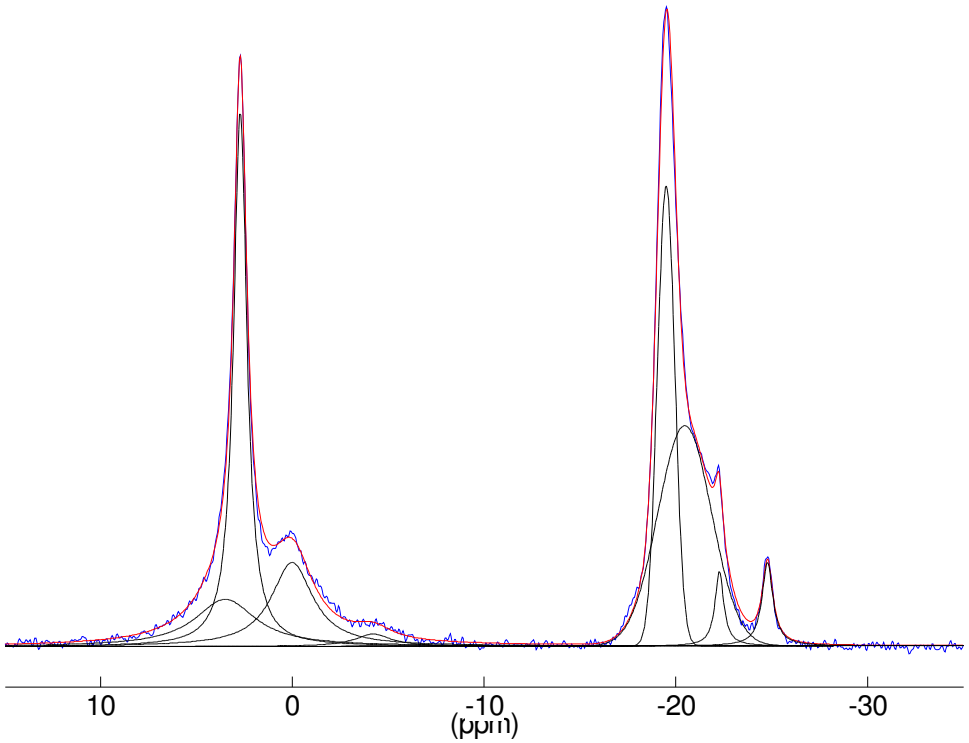

SI-6. Deconvoluted {^{1}H}-^{31}P CP MAS spectra of *ZH4* at 2 ms contact time

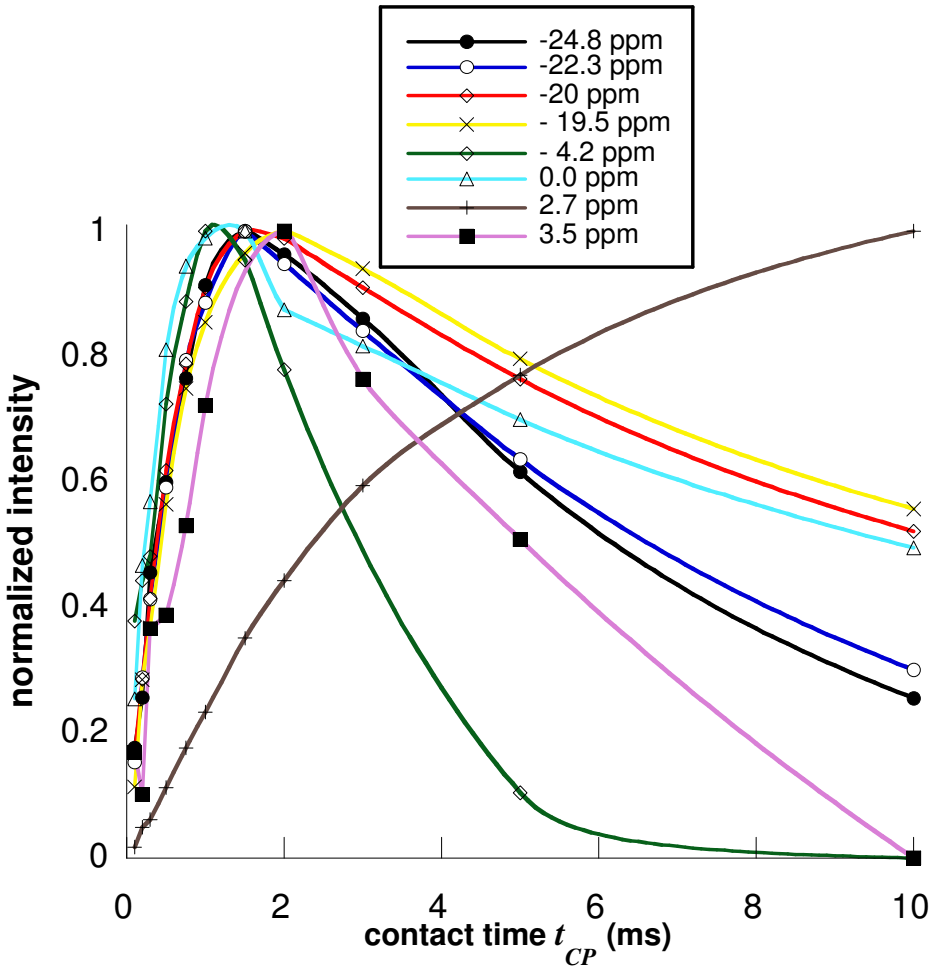

SI-7. Evolution of the normalized intensity of selected signals of ZH4 as a function of contact time from deconvoluted {^{1}H}-^{31}P CP MAS spectra.

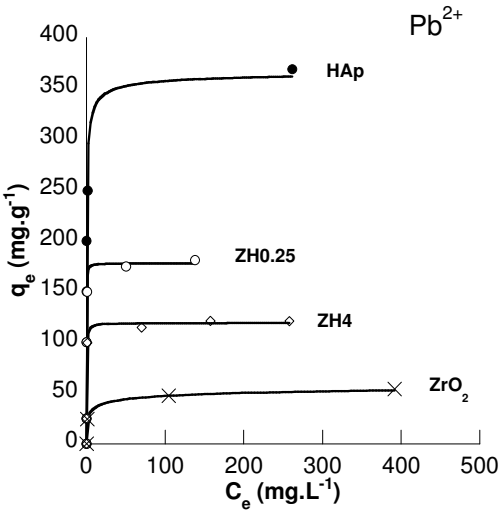

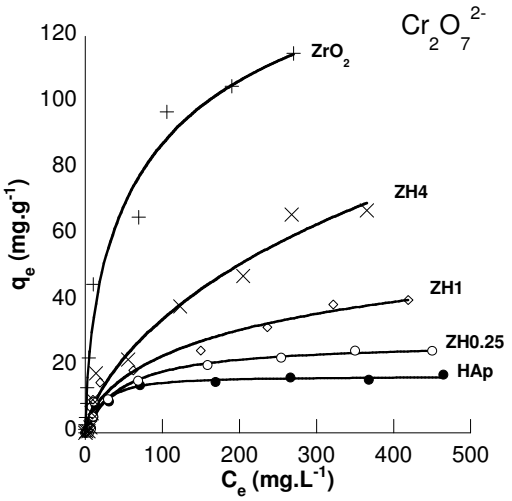

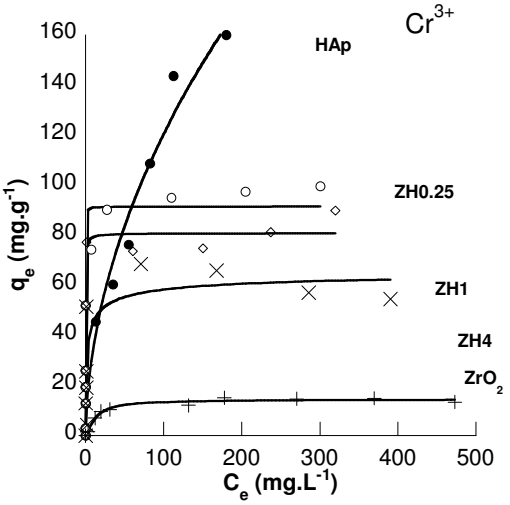

The plain curves correspond to the fitting of exprimental data using a Freundlich-type model :

$$\frac{q_e}{q_{e,max}} = \frac{\alpha . C_0^{\beta}}{1 + \alpha . C_0^{\beta}}$$

with q_e the amount of adsorbed metal at equilibrium for an initial concentration C_0 and $q_{e,max} = q_e$ when $C_0 \rightarrow \infty$ (*i.e.* adsorption capacity). α and β are two constants related to the adsorbent-adsorbate interactions (from Otake, Y. ; Kalili, N. ; Chang, T. H. ; Furuya, E. *Separ. Purif. Technol.* **2004**, *39*, 67-72)

SI-8. Result of metal sorption data fitting using a Freundlich-type model